CHAPTER 6

Emission Source Quantification

Emission source quantification (ESQ) plays a vital role in the methane measurement and mitigation process, as well as, provides a way to verify carbon credits from engineering controls and technologies used to capture methane (e.g. biogas digestors). In this chapter, we will overview the conventional and sUAS-based advanced leak detection and quantification (LDAQ) methodology. The LDAQ methods utilize several concepts and approaches within numerics, control, and optimization as well as approaches based on different available sensing modalities (see Fig. 6.1 for effective length-scales). In this chapter, we divided these approaches into five general categories, namely: Simulation-based (Section 6.1.1), Optimization-based (Section 6.1.2), Mass-Balance-based (Section 6.1.3), Imaging-based (Section 6.1.4), and Correlation-based (Section 6.1.5).

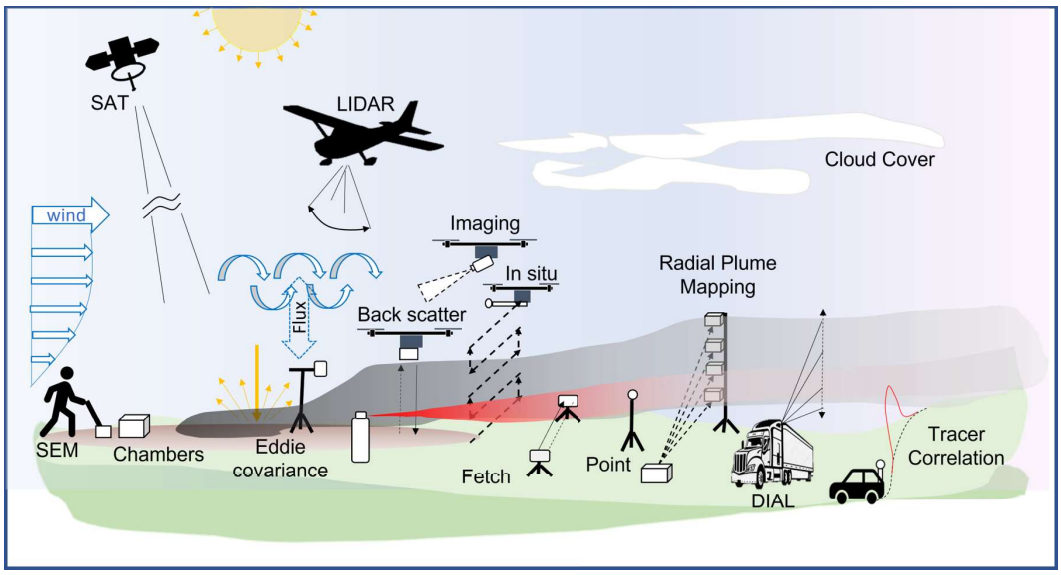

Figure 6.1 Leak detection and quantification methods and modalities.

6.1 TYPES OF QUANTIFICATION APPROACHES

In the Simulation-based approaches, the methods depend heavily on simulation and computational tools for solving dynamic partial differential equations, which are used to determine the source rate estimation. Sometimes other source parameters are also estimated in the process and this is typically referred to as source term estimation (STE) or the source determination problem (SDP). Two methods that show up in the literature are backwards Lagrangian stochastic (bLS) and mesoscale recursive Bayesian least squares inverse (RB-LSI).

The optimization-based methods showcased in this manuscript depend on some form of a parameterized system model, which undergoes a model fitting or recursive optimization (statistical or information based). Many of these methods include several variations of the point source Gaussian (PSG) solution of the classical Gaussian plume model. This is seen in the PSG approach based on the EPA's other test method (OTM) 33A, where the data is gathered from a single sensor downwind and undergoes model fit of the peak concentration measured.

Next is the conditionally sampled PSG (PSG-CS) approach that utilizes meteorological data in the model fitting process using conditionally sampled concentration data based on the incremental changes in wind direction. Another variation to this is the recursive Bayesian PSG (PSG-RB) that utilizes a moving sensor and meteorological data to condition the models likelihood function and prior for updating the posterior distribution that is used to quantify the source estimate. This approach also considers past knowledge about equipment characteristics if this is known.

A different approach to the Bayesian way of thinking is to solve for the parameters of the model conditioned on the observations. This approach also utilizes a particle filter and Markov Chain Monte Carlo (MCMC) to update the posterior and is referred to as the PSG sequential Bayesian MCMC (PSG-SBM). The last optimization approach mentioned is the Near-Field Gaussian Plume Inversion (NGI) and the modified NGI approach.

The NGI utilizes fitting the Gaussian plume model based on sampling of a perpendicular plane downwind of the source. The vertical and horizontal dispersion relations are used to find the center of the plume within the perpendicular plane and minimize, by least square fit, the difference between the modeled concentration and the observed concentration (integrated over the lateral dispersion direction).

The next category is the Mass-Balance-based approaches, which includes methods that utilize equations based on mass conservation and continuity. The simplest approach is the vertical flux plane (VFP), which takes a control volume approach to estimating the emission rate by measuring the flux entering and leaving the control volume. Traditionally, the plume is sampled using a raster scanning approach in a perpendicular plane upwind and downwind of the source. The sparse set of observations within the plane undergo a spatial interpolation process and are combined with the wind to estimate the source rate.

A direct variation to this approach is the cylindrical flux plane (CFP), which the sensing system measures concentrations on successive loops around the source at different altitudes. The flux going into and out of this cylindrical plane is used to

estimate the flux. Using different sensing modalities (such as imaging or backscatter-based sensors), a path integrated vertical flux plane (PI-VFP) method can be formulated. Both aircraft and sUAS-based approaches to PI-VFP have been implemented, which rely on horizontal scanning of the area of interest.

For sUAS-based PI-VFP, concentric circles are flown to confirm that sources are contained inside the path before estimating the source rate. A flux plane approach has also been explored using a series of TDLAS-based laser fetches at different altitudes and utilizes the time-average of the line-integral of the instantaneous product of the wind speed and concentration. This is advantageous to other VFP approaches as it provides very good performance and does not take time to scan the plane. However, it is in ways impractical as it requires setup of the laser fetches and knowledge of the source geometry.

The next method is the Gauss divergence theorem (GDT) approach. It utilizes the CFP approach with mass flux continuity as well as the expected time rate of change of the mass within the control volume to estimate the source rate. Another VFP approach was included in this review that uses Gaussian plume model optimization with a general linear model (GLM) to help determine the contributions of multiple sources. This approach is referred to as the VFP-GLM.

The last Mass-Balance-based approach is vertical radial plume mapping (VRPM). The VRPM approach uses a ground based laser with retro-reflectors at different altitudes downwind of the source. The path integrated concentrations are measured at different radial angles and used to estimate the flux.

The next category is the Imaging-based approaches that utilize MWIR, hyperspectral cameras, and absorption spectroscopy (such as iterative maximum a posteriori differential optical absorption spectroscopy (IMAP-DOAS)).

The last category covered in this manuscript is the correlation-based approaches, which includes the traditional Eddy covariance (EC) method (in brief) and the tracer correlation method (TCM). The TCM has also been referred to in the literature as the tracer dispersion method (TDM) and atmospheric tracer method (ATM).

6.1.1 Simulation-based

6.1.1.1 Forward Modeling

Forward modeling is typically used for projecting or forecasting dispersion. Forward modeling is not directly used in emission quantification by itself, but rather paired with feedback in the optimization sense. This can include numerically solving a governing set of equations, such as the advection diffusion equation (ADE) or applying a parameterized general model (such as the Gaussian plume). It is also common in practice to utilize existing numerical models, such as the WindTrax 2.0, WRF model, FLEXible PARTicle-Weather Research and Forecasting (FLEXPART-WRF), SCIPUFF, QUIC, and others that can be Lagrangian-base, include turbulence e.g., Large eddie simulation (LES), and Reynolds averaged Navier Stokes (RANS). Interested readers can check the review paper from [53] on dispersion models.

6.1.1.2 Backward Lagrangian Stochastic (bLS)

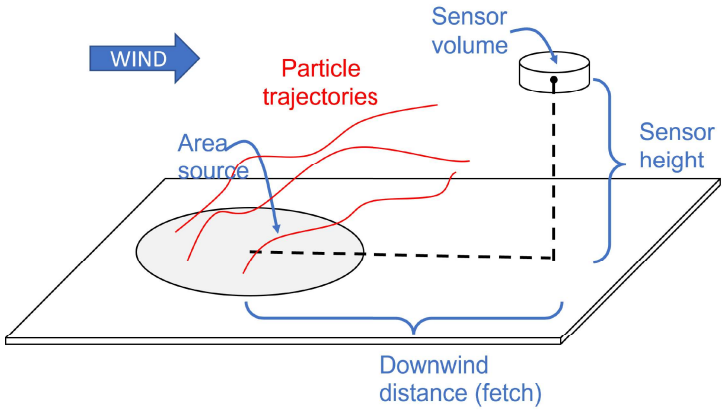

Figure 6.2 A diagram depicting the bLS approach (e.g. see [35]).

The accepted backward modeling approach used in the draft OTM- 33A document [33] and in several applications (e.g., Dairy Farm [8], etc.) is the backwards Lagrangian stochastic (bLS) approach by [35]. The bLS approach aims to answer the general questions: What is the proper form of the LS trajectory model? As well as, how can source estimates be extracted from the particle's backward LS trajectory? The forward model, formulated as a generalized Langevin equation, is evolved jointly as a Markov process,

$$du_i = a_i(\mathbf{x}, \mathbf{u}, t)dt + b_{i,j}(\mathbf{x}, \mathbf{u}, t)d\xi_j, \quad dx_i = u_i dt, \tag{6.1}$$

where the particle position is given by $\mathbf{x} = (x_1, x_2, x_3)$, and $d\xi_j$ is a random increment governed by a Gaussian process. The functions a_i and $b_{i,j}$ have to be specified such that the velocity probability density function, $g_a(\mathbf{x}, \mathbf{u}, t)$, satisfies the Fokker–Planck equation (FPE) [35],

$$\frac{\partial g_a}{\partial t} = \frac{\partial}{\partial x_i}(u_i, g_a) - \frac{\partial}{\partial u_i}[a_i(\mathbf{x}, \mathbf{u}, t)g_a] + \frac{\partial}{\partial x_i}[B_{i,j}(\mathbf{x}, \mathbf{u}, t)g_a]. \tag{6.2}$$

This method provides a source estimation for an area source given the source location (with unknown source rate), assuming horizontally uniform surface source, and that the atmosphere is in horizontal equilibrium (see Fig. 6.2). To make an emission estimate using bLS, the method utilizes the dispersion model relation,

$$\frac{Uy}{Q} = n = f(\mathbf{x}_m, \mathbf{x}_0, L, h, G), \tag{6.3}$$

where U is the wind speed, y is the measured concentrations, Q is the source rate, L is the Monin–Obukhov length, h is the depth of the mixing layer, G describes the set of parameters characterizing the plume, and x_{3m} represents the measurement height. As the particles from the back trajectories touchdown in the source area, the vertical

velocities, w_0 are logged and used to estimate n,

$$n(x_{3m}) = \frac{y(x_{3m})U(x_{3m})}{Q} = \frac{1}{N}\sum \Big|\frac{2}{w_0/U(x_{3m})}\Big|. \tag{6.4}$$

Once n is known, an estimate of the source rate can be determined using the measured concentration and wind speed, $Q = n/(yU)$. In this approach, due to the time-averaged ensemble, the accuracy improves over time (nominal averaging period of 15 min [35]). An alternate expression for the emission estimate is given as

$$Q_{bLS} = \frac{y - y_b}{(y/Q)_{sim}}, \tag{6.5}$$

where y_b is the background concentration and $(y/Q)_{sim}$ is calculated using

$$(y/Q)_{sim} = \frac{1}{N}\sum |\frac{2}{w_0}|. \tag{6.6}$$

This Monin–Obukhov similarity theory (MOST)-based bLS emission estimation methodology was validated against the mass balance approach (given the along-wind distance of the source d),

$$Q_m = \frac{1}{d}\int_0^\infty y(x_3)U(x_3)dx_3, \tag{6.7}$$

and field tested in [34, 37, 36]. A lagoon environmental leak was simulated and explored with the bLS approach by constructing a large 45 m by 45 m emission source on a pond. The accuracy was shown to be lower during the summer period due to more frequent unstable atmospheric conditions [72].

6.1.1.3 Mesoscale Recursive Bayesian Least Squares Inverse (RB-LSI)

Utilizing the NOAA P-3 aircraft and a wavelength-scanned CRDS, [23] used a mesoscale bayesian least squares approach to solve the inverse problem of estimating emissions. They use the FLEXPART-WRF to model the forward problem, which was compared to physical observations and minimized on an iterative cost function that assumes lognormal distributions,

$$\begin{aligned} J = &\frac{1}{2}(\ln(y_0) - \ln(Hx))^T(\ln(y_0) - \ln(Hx)) \\ &+\frac{1}{2}\alpha(\ln(x) - \ln(x_b))^T(\ln(x) - \ln(x_b)), \end{aligned} \tag{6.8}$$

where the observed concentration enhancements are given as y_0, posterior solutions are x, FLEXPART-WRF outputs are H, prior fluxes are x_b, error covariance matrix from observations are R, and error covariance matrix from prior fluxes are B in the lognormal space.

6.1.2 Optimization-based

In this section, we discuss the emission quantification techniques that utilize some form of optimization in the methodology that fits a model.

6.1.2.1 Point Source Gaussian (PSG) - OTM33A

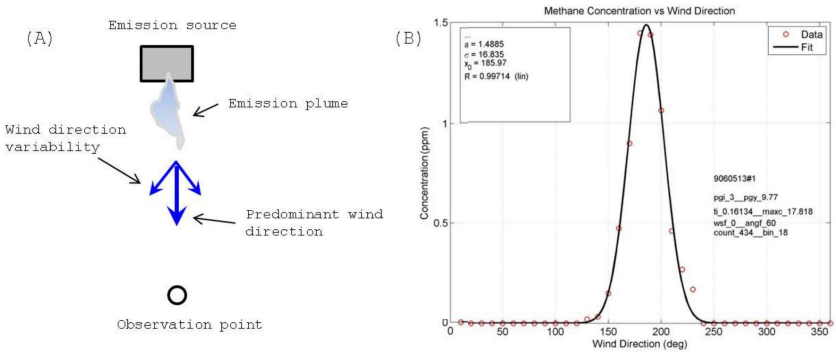

Figure 6.3 (a) Depiction of Gaussian plume dispersion with an observer making a stationary measurement downwind. (b) Resulting time-integrated data with a Gaussian fit applied [33].

In [33], the point source Gaussian (PSG) is discussed. The measurement involves a vehicle with a concentration measurement instrument (CMI) to park downwind of the known source with the vehicle off. The CMI (such as Picarro or LGR UGGA) collects data at roughly 2.5 m above ground at a known distance from the source. The variations in the wind direction are measured using a sonic anemometer (e.g., R.M. Young). The PSG calculations are based off of enhanced emission levels and can be calculated as the fifth percentile of the concentration time series signal. The PSG estimate then becomes a simple 2-D Gaussian integration with no reflection term. The source estimate is given as,

$$Q_E = 2\pi\sigma_{x_2}\sigma_{x_3}U_m y_p, \tag{6.9}$$

where y_p is the peak concentration from the Gaussian fit, U_m is the mean wind speed, σ_{x_3} and σ_{x_2} are the vertical and lateral plume dispersion that can be determined from the meteorological conditions, such as the Pasquill–Gifford stability classification curves [54] (see Fig. 6.3). The accuracy of the OTM33A method is explored in [30, 31].

6.1.2.2 Conditionally Sampled PSG (PSG-CS)

To capture the ensemble mean of the downwind plume behavior, a dispersion model is used in [39], where we denote $\mathbf{x} = [x_1, x_2, x_3]^T$ is the downwind distance, crosswind distance ($x_2 = 0$ is the plume center) and vertical position, respectfully. The model is a function of downwind distance and dispersion factors $D_{x_2}(x_1, x_2)$ and $D_{x_3}(x_1, x_3)$,

given as,

$$y_m(\mathbf{x}) = \frac{Q}{\overline{U}} D_{x_2}(x_1, x_2) D_{x_3}(x_1, x_3). \tag{6.10}$$

This method essentially aims to determine the source rate, Q, using the conditional mean concentration data, y_m, of the downwind plume. The lateral dispersion downwind of a continuous point source can be shown to have a Gaussian distribution such that it can be represented as,

$$D_{x_2}(x_1, x_2) = \frac{1}{\sqrt{2\pi}\sigma_{x_2}} [-\frac{1}{2}(\frac{x_2}{\sigma_{x_2}}^2)]. \tag{6.11}$$

However, the vertical dispersion (assuming vertical eddy diffusivity and wind speed that scales vertically to a power law) can be formulated as a parameterized stretched exponential (originally expressed in [84]),

$$D_{x_3} = D_{x_3}(x_1, x_3) = \frac{A}{\overline{x_3}} \exp\left[-(\frac{B x_3}{\overline{x_3}})^s\right]. \tag{6.12}$$

The parameters $\overline{x_3}$, s, A, and B are functions of the atmospheric stability and downwind distance, x_1. A and B can be described using the usual Gamma function, $\Gamma(\cdot)$ as,

$$A = s\Gamma(2/s)[\Gamma(1/s)]^2, \tag{6.13}$$

$$B = s\Gamma(2/s)\Gamma(1/s). \tag{6.14}$$

The conditional averaged concentration can be calculated using,

$$\langle y|\theta\rangle = \frac{1}{n} \sum_{\theta_i \in \Theta}^{n} y(\theta_i), \tag{6.15}$$

where the set $\Theta(\theta) = \{\theta_i : |\theta - \theta_i| < \Delta\theta/2, \forall i = 1, 2, ..., n\}$ and $\Delta\theta = 2^\circ$. The basic idea is to capture the plume geometry in the crosswind direction, which is further used to derive the least squares source estimate,

$$Q = \Big[\sum_{i=1}^{N} \frac{D_{x_2} D_{x_3}}{\overline{U}} \langle y|\hat{d}_i\rangle\Big] / \Big[\sum_{i=1}^{N} (\frac{D_{x_2} D_{x_3}}{\overline{U}})^2\Big]. \tag{6.16}$$

As shown in [39], the lateral dispersion can be determined in two ways: classically, using atmospheric stability (for constants a_{x_2} and p_{x_2}) [29],

$$\sigma_{x_2} = a_{x_2} x_{3_0} 1.9 (L_x / x_{3_0})^{p_{x_2}}; \tag{6.17}$$

and by reconstructing the lateral dispersion,

$$\sigma_{x_2} = \sqrt{\frac{1}{N} \sum_{i=1}^{N} \underline{\hat{d}}_i}, \tag{6.18}$$

where the N is the number of values in $\langle y|\underline{\hat{d}}\rangle$, and $\underline{\hat{d}}$ are $\hat{d}$ values that are greater than the minimum concentration (i.e., background) and $\pm 40°$ off the plume center θ_p. The distance $\hat{d}$ is calculated as,

$$\hat{d}(\theta) = L_x \sin(\theta - \theta_p), \tag{6.19}$$

with $\theta_p = \arg\max_\theta \langle y|\theta\rangle$ (see Figure 6.4).

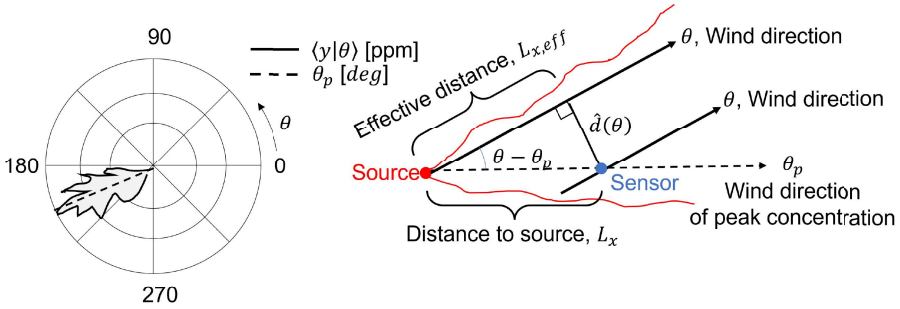

Figure 6.4 (left) Polar plot with the wind direction, θ as the radial axis, and the conditionally averaged concentration, $\langle y|\theta\rangle$ as the distance from the center. θ_p is the peak wind direction located at the maximum conditionally averaged concentration. (right) Illustration of the wind direction geometry for conversion of θ to crosswind position $\hat{d}$ with the source plume represented by the dashed lines [39].

6.1.2.3 *Recursive Bayesian Point Source Gaussian Method (PSG-RB)*

In work from [2, 47], a moving sensor measured a point source concentration that can be formulated as,

$$y(\mathbf{x}) = \frac{Q}{\overline{U}} D_{x_2}(x_1, x_2) D_{x_3}(x_1, x_3). \tag{6.20}$$

The source rate is given as Q, the effective wind speed is $\overline{U}$, and the lateral and vertical dispersion is characterized by $D_{x_2}(x_1, x_2)$ and $D_{x_3}(x_1, x_3)$, respectfully. The equation is formulated such that the downwind distance, x_1, is aligned with the predominant wind direction. Since the measurement is taken at closer distances to the source, the lateral dispersion is taken as a random function such that,

$$\int_{-\infty}^{\infty} D_{x_2}(x_1, x_2) dx_2 = 1. \tag{6.21}$$

This can be advantageous for instantaneous plumes. The integrated lateral concentration can be written as,

$$y^{x_2}(x_1, x_3) = \frac{Q}{\overline{U}} D_{x_3}(x_1, x_3). \tag{6.22}$$

The choice of the vertical dispersion D_{x_3} (originally expressed in [84]) is that of a parameterized stretched exponential function,

$$D_{x_3} = D_{x_3}(x_1, x_3) = \frac{A}{\overline{x_3}} \exp\left[-\left(\frac{Bx_3}{\overline{x_3}}\right)^s\right], \tag{6.23}$$

where $\overline{x_3}$, s, A, and B are functions of atmospheric stability and downwind distance, x_1. The lateral dispersion is given as

$$D_{x_2} = \frac{1}{\sqrt{2\pi}\sigma_{x_2}} \exp\left[-\frac{1}{2}\left(\frac{x_2}{\sigma_{x_2}}\right)^2\right]. \tag{6.24}$$

Then, by numerically integrating (6.20) and incorporating the vehicle movement V,

$$y^{x_2} = \sum_{i=0}^{\infty} y(\mathbf{x}_i)\Delta t V = Q \sum_{i=0}^{\infty} \frac{\Delta t V}{\overline{U}_i} D_{x_3}(x_{1_i}, x_{3_i}) D_{x_2}(x_{1_i}, x_{2_i}). \tag{6.25}$$

The recursive Bayesian approach described here is based on well pads and oil and gas production, which are used to help inform the path planning of the mobile sensor. For brevity, we will only cover the formulation of the quantification only. Starting with the definition of the posterior distribution,

$$p(Q|M, W, \Lambda) = \frac{p(Q|W)p(M|Q, \Lambda)}{p(M|\Lambda)}, \tag{6.26}$$

where M is the concentration data, W is the ancillary information (e.g., well pad characteristics), Λ is the meteorological conditions, $p(Q|W)$ is the prior, $p(M|Q, \Lambda)$ is the likelihood, and $p(M|\Lambda)$ is the evidence (which can be thought of as a normalization constant for the likelihood [91]). The prior is given as

$$p(Q|W) = \frac{1}{\beta} \exp\Big[-\left(1 + \gamma\frac{Q-\mu}{\beta}\right)^{-\frac{1}{\gamma}}\Big]\Big(1 + \gamma\frac{Q-\mu}{\beta}\Big)^{-1-1/\gamma}, \tag{6.27}$$

where the hyperparameters need to be fit to the application (for well-pad source, $\gamma = 1$, $\mu = 0.19$, $\beta = 0.23$ based on [14]). The likelihood function is chosen to be a Gaussian,

$$p(M|Q, \Lambda) = \frac{1}{\sqrt{2\pi}\sigma_e} \exp\Big[-\frac{1}{2}\Big(\frac{y^{x_2} - y^{x_2,M}}{\sigma_e}\Big)^2\Big], \tag{6.28}$$

where $y^{x_2,M}$ is the modeled concentration for a given source rate, and σ_e is the combined model and measurement error (outlined in [90]). The recursive approach involves replacing the prior with the previous posterior distribution found using the likelihood function,

$$p(Q|W)_i = \begin{cases} p(Q|W), & i = 1, \\ p(Q|M, W, \Lambda)_{i-1}, & i > 1. \end{cases} \tag{6.29}$$

As the number of passes increases, the posterior distribution improves and can be used to estimate the source rate,

$$\hat{Q} = \int_{Q_{min}}^{Q_{max}} Qp(Q|M, W, \Lambda)dQ. \tag{6.30}$$

Variations of this method were seen in [47], where the measurement noise was assumed to be Gaussian and also included a UAV with sensor noise and utilized the flux plane mass balance method to estimate the source rate, which was used in the calculation of the posterior distribution. Further field tests of this method were carried out in [93].

6.1.2.4 *Point Source Gaussian Sequential Bayesian Markov Chain Monte Carlo (PSG-SBM)*

Utilizing the Gaussian plume model for the likelihood of a sequential Bayesian Markov Chain Monte Carlo (MCMC) method, a UAV scans horizontally to update the estimated posterior distribution in [55]. The parameters are given as Θ_k where $\Theta_k = [\mathbf{x}_s^T, Q_s, u_s, \phi_s, \zeta_s]^T$, the position is $\mathbf{x}_s$, source rate Q_s, wind speed and direction u_s and ϕ_s, and the model diffusion coefficients $\zeta_s = [\zeta_{s1}, \zeta_{s2}]^T$. The point source observations, $\mathbf{y}_{1:k} = \{y_1, y_2, ..., y_k\}$ are used within Bayes rule to update the posterior,

$$p(\Theta_{k+1}|\mathbf{y}_{1:k+1}) = \frac{p(\mathbf{y}_{k+1}|\Theta_{k+1})p(\Theta_{k+1}|\mathbf{y}_{1:k})}{p(y_{k+1}|\mathbf{y}_{1:k+1})}. \tag{6.31}$$

The likelihood model, $\mathcal{M}(\mathbf{x}_k, \zeta_k)$, in [55], based on observational data, $\overline{y}_k = \mathcal{M}(\mathbf{x}_k, \zeta_k) + \overline{v}_k$, was taken to be detection event, $p(\overline{y}_k|\Theta_k)$, if $y_k > y_{thr}$,

$$p(\overline{y}_k|\Theta_k) = \frac{1}{\sigma_k\sqrt{2\pi}} \exp\Big[- \frac{(\overline{y}_k - \mathcal{M}(\mathbf{x}_k, \zeta_k))^2}{2\sigma_k^2}\Big], \tag{6.32}$$

and a non-detection event otherwise,

$$p(\underline{y}_k|\Theta_k) = (\frac{p_b}{2}[1 + \text{erf}\Big(\frac{y_{thr} - \mu_b}{\sigma_b\sqrt{2}}\Big)]) + p_m + (\frac{p_s}{2}[1 + \text{erf}\Big(\frac{y_{thr} - (\mu_b + \mathcal{M}(\mathbf{x}_k, \zeta_k))}{\sigma_b\sqrt{2}}\Big)]). \tag{6.33}$$

The three terms in the non-detection event account for instrument noise, turbulence, and observing concentrations above the threshold, where $p_b + p_m + p_s = 1$, and μ_b and σ_b are mean background noise and standard deviation, respectively. Using a particle filter, the posterior can be approximated by a set of n weighted random samples $\{\Theta_k^{(i)}, w_k^{(i)}\}_{i=1}^n$,

$$p(\Theta_k|\overline{y}_{1:K}) \approx \sum_{i=1}^{n} w_k^{(i)} \delta(\Theta_k - \Theta_k^{(i)}), \tag{6.34}$$

where δ is the Dirac delta function. The un-normalized weights are then updated using

$$\overline{w}_{k+1}^{(i)} = w_k^{(i)} \cdot p(y_{k+1}|\Theta_{k+1}^{(i)}). \tag{6.35}$$

Once the weights are determined they can be normalized by dividing by the summation of all the weights. Additionally, an effective sample size must be considered to avoid the degeneracy problem. The new samples undergo a MCMC step that is accepted with the likelihood probability distribution described earlier (see more details in [55]).

6.1.2.5 Near-Field Gaussian Plume Inversion (NGI)

The near-field Gaussian plume inversion (NGI) method [76, 1] is a mass continuity model in principle, where the upwind and downwind concentration measurements, combined with wind measurements, of an emission source are differenced to quantify emission flux. The NGI method is typically sampled around 100 m from the source. The sampling aims to capture the time-invariant behavior of the plume, which, under turbulent conditions, may not map out the characteristic Gaussian plume shape.

This is because it is assumed that spatial variability in the time-averaged plume is Gaussian. This method was initially carried out with a DJI S900 equipped with a ultra portable greenhouse gas analyzer (UGGA) by Los Gatos Research Inc. (LGR). The flux estimate is derived by fitting the experimentally measured flux values, q_{me}, to the modeled flux values, q_{m0} given as,

$$q_{me} = (y - y_b)U(x_3)\rho, \tag{6.36}$$

where the modeled flux is given by the Gaussian model,

$$q_{m0} = \frac{Q_e}{2\pi\sigma_{x_2}(x_1)\sigma_{x_3}(x_1)} \exp\left(\frac{-(x_2 - x_{2c})^2}{2\sigma_{x_2}(x_1)^2}\right)\left(\exp\left(\frac{-(x_3 - h)^2}{2\sigma_{x_3}(x_1)^2}\right) + \exp\left(\frac{-(x_3 + h)^2}{2\sigma_{x_3}(x_1)^2}\right)\right). \tag{6.37}$$

The lateral and vertical dispersion relations are typically looked up in the PGT stability tables, however, in this method, they are assumed to be linearly proportional to downwind distance,

$$\tau_{x_2} = \sigma_{x_2}(x_1)/x_1, \quad \tau_{x_3} = \sigma_{x_3}(x_1)/x_1. \tag{6.38}$$

Trying to solve (6.37) is not always well constrained, and thus the method proposes to separate (6.37) and fit the model along the x_3-direction,

$$q_{me,x_2} = q_{me}\frac{\tau_{x_3}x_1\sqrt{2\pi}}{\left(\exp\left(\frac{-(x_3-h)^2}{2(\tau_{x_3}x_1)^2}\right) + \exp\left(\frac{-(x_3+h)^2}{2(\tau_{x_3}x_1)^2}\right)\right)}. \tag{6.39}$$

The spatial variability in the x_3-direction has to be sampled to determine τ_{x_3}. The lateral spatial variability τ_{x_2} and plume center x_{2c} are determined simultaneously,

$$x_{2c} = \frac{\sum_j (q_{me,x_2}x_{2j})}{\sum_j (q_{me,x_2})}, \tag{6.40}$$

$$\tau_{x_2} = \sqrt{\frac{\sum_j (q_{me,x_{2j}} (\frac{x_{2j} - x_{2c}}{x_{1j}})^2)}{\sum_j (q_{me,x_{2j}})}}. \tag{6.41}$$

Once the unknowns, τ_{x_3}, τ_{x_2}, and x_{2c} are determined, the source emission rate, $\hat{Q}$, can be estimated by minimizing the least square fit between q_{me} and q_{mo}, parameterized by Q_e and τ_{x_3}. The uncertainty in $\hat{Q}$ and the impact of limiting τ_{x_3} are given in [76].

6.1.2.6 Modified NGI

To improve the optimization routine of the NGI method, the modified NGI (mod-NGI) method looks at conditioning the parameter estimates by using the following flux-based likelihood function, represented by,

$$P(q|\theta) = D_{x_2}(x_1, x_2; \sigma_{x_2}, \mu_{x_2}) D_{x_3}(x_1, x_3; \sigma_{x_3}, \mu_{x_3}), \tag{6.42}$$

where $\theta = [Q, \mu_{x_2}, \mu_{x_3}, \sigma_{x_2}, \sigma_{x_3}]^T$ and the dispersion functions are,

$$D_{x_2}(x_1, x_2; \sigma_{x_2}, \mu_{x_2}) = \frac{1}{\sqrt{2\pi}\sigma_{x_2}(x_1)} \exp\left(\frac{-(x_2 - \mu_{x_2})^2}{2\sigma_{x_2}(x_1)^2}\right), \tag{6.43}$$

$$D_{x_3}(x_1, x_3; \sigma_{x_3}, \mu_{x_3}) = \frac{\exp\left(\frac{-(x_3 - \mu_{x_3})^2}{2\sigma_{x_3}(x_1)^2}\right) + \exp\left(\frac{-(x_3 + \mu_{x_3})^2}{2\sigma_{x_3}(x_1)^2}\right)}{\sqrt{2\pi}\sigma_{x_3}(x_1)}. \tag{6.44}$$

When the source rate is multiplied we have the modelled flux equation,

$$q_{mo} = \mathcal{M}(\mathbf{x}, \theta) = Q D_{x_2}(x_1, x_2; \sigma_{x_2}, \mu_{x_2}) D_{x_3}(x_1, x_3; \sigma_{x_3}, \mu_{x_3}). \tag{6.45}$$

Consider that experimental measurements do not give access to the above likelihood function but can rather give an estimate of it and let's assume an initial source rate estimate $\hat{Q}$ such that,

$$\hat{P}(q_{me}|\hat{\theta}) \approx \frac{Q}{\hat{Q}} D_{x_2}(x_1, x_2; \hat{\sigma}_{x_2}, \hat{\mu}_{x_2}) D_{x_3}(x_1, x_3; \hat{\sigma}_{x_3}, \hat{\mu}_{x_3}). \tag{6.46}$$

The likelihood of observing the entire dataset then becomes,

$$\hat{P}(D|\hat{\theta}) = \Pi_{i=1}^{N} \hat{P}(q_{me}^i|\hat{\theta}). \tag{6.47}$$

Given that analytically solving for an optimizer using (6.44) can be complex, we make the assumption that the plume is far from the ground only for the parameter initialization steps. This allows for the approximation of (6.44) by,

$$D_{x_3}(x_1, x_3; \hat{\sigma}_{x_3}, \hat{\mu}_{x_3}) \approx \frac{1}{\sqrt{2\pi}\sigma_{x_3}(x_1)} \exp\left(\frac{-(x_3 - \mu_{x_3})^2}{2\sigma_{x_3}(x_1)^2}\right). \tag{6.48}$$

Solving for the maximum log likelihood estimate (MLE) yields,

$$\hat{\tau}_{x_2} = \sqrt{\frac{1}{Nx_1^2}\sum_{i=1}^{N}(x_{2i} - \mu_{x_2})^2}, \quad \hat{\tau}_{x_3} = \sqrt{\frac{1}{Nx_1^2}\sum_{i=1}^{N}(x_{3i} - \mu_{x_3})^2}. \tag{6.49}$$

It can be readily apparent that the MLE is the definition of the standard deviation conditioned only on the spatial coordinates. To make this MLE conditioned on the flux measurements one can substitute for the weighted standard deviation. For example, the horizontal scale factor is given by,

$$\hat{\tau}_{x_2} = \sqrt{\frac{N}{(N-1)x_1^2}\frac{\sum_{i=1}^{N} q_{me}^i (x_{2i} - \mu_{x_2})^2}{\sum_{i=1}^{N} q_{me}^i}}. \tag{6.50}$$

In order to estimate τ_{x_2} and τ_{x_3}, the plume centers need to be computed. This is done using the measured flux as weights, and computing the center of mass,

$$\hat{\mu}_{x_2} = \frac{\sum_{i=1}^{N} q_{me}^i x_{2i}}{\sum_{i=1}^{N} q_{me}^i}, \quad \hat{\mu}_{x_3} = \frac{\sum_{i=1}^{N} q_{me}^i x_{3i}}{\sum_{i=1}^{N} q_{me}^i}. \tag{6.51}$$

Alternatively, the plume widths can be estimated directly without knowledge of plume location,

$$\hat{\sigma}_{x_2} = \sqrt{\frac{N}{(N-1)}\frac{\sum_{i=1}^{N} q_{me}^i (x_{2i} - \mu_{x_2})^2}{\sum_{i=1}^{N} q_{me}^i}}, \tag{6.52}$$

and similarly for σ_{x_3}. Once the dispersion and plume center parameters are estimated and a initial estimate of the source rate is established for $\hat{Q}$, the optimization of parameters θ can be undertaken, such that,

$$\hat{\theta} = \min_{\theta} \; J(\mathbf{X}, \theta), \quad J(\mathbf{X}, \theta) = \frac{1}{N}\sum_{i=1}^{N}(\mathcal{M}(\mathbf{x}_i, \theta) - q_{me}^i)^2, \tag{6.53}$$

where $\mathbf{X}$ is the observation data set $\mathbf{X} = [\mathbf{x}_1, \mathbf{x}_1, \cdots, \mathbf{x}_N]$. This optimization can be carried out using the MATLAB *fminsearchbnd* function [27].

6.1.3 Mass Balance-based

The mass balance approach aims to estimate an emission source by balancing the mass flux leaving or entering a control volume. Generally, there are two path planning approaches to the mass balance method: (1) rectangular vertical flux plane (or curtain) downwind of the source and (2) a cylindrical flux plane enclosing the source. For a well behaved plume under stable atmospheric conditions, the downwind plume contains all the flux. The sampling distance from the source may vary based on each submethod. The measured flux plane data can be sparse and is typically subject to spatial interpolation.

6.1.3.1 *Vertical Flux Plane (VFP)*

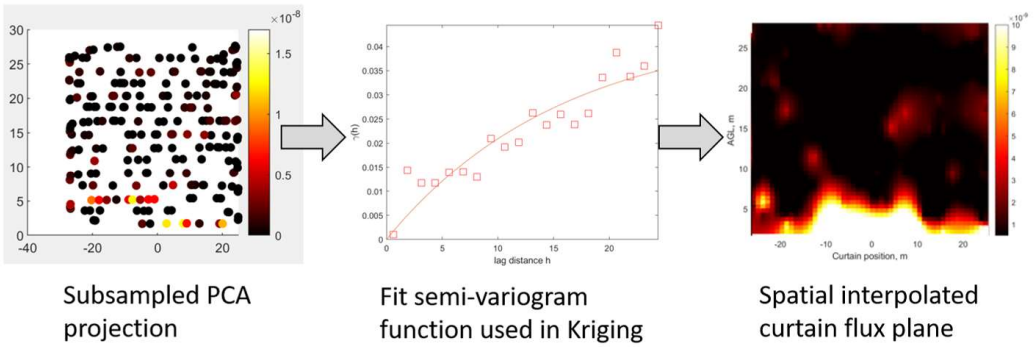

Figure 6.5 Demonstration of using sampled flux plane data and applying kriging to it for spatial interpolation [52].

The flux plane method generally involves sampling within a plane, vertically or horizontally, upwind and downwind, of an emission source. It has been applied in several works [6, 5, 19, 18, 41, 51, 65, 70, 71, 77, 78, 88, 87, 86, 13]. The plane is typically sampled using a raster-scanning approach, capturing the plume within the width and height of the plane. The emission rate (in moles s^{-1}) can be estimated as,

$$Q_c = \iint_{\Omega_p} n_{ij}(y - y_b)\mathbf{u} \cdot \hat{\mathbf{n}}_f dx_2 dx_3, \tag{6.54}$$

where n_{ij} is the mole density of air (given standard temperature and pressure), $(y - y_b)$ is the enhanced mole fraction (referenced to air), y_b is the background mole fraction, $\mathbf{u}$ is the wind speed vector, and $\hat{\mathbf{n}}_f$ is the flux plane normal vector (see Fig. 6.5). Since the measurements are sparse, the integral irregularly spaced. To combat this, the sparsely sampled points are spatially interpolated using techniques, such as inverse distance weighting (IDW) [22] or kriging [85]. This is a common problem in geostatistics to interpret unknown data, $y(\mathbf{x}_0)$, from desired spatial locations $\mathbf{x}_0$ in domain $\Omega \in \mathbb{R}^2$ (in our case is the domain of the plane $\Omega_p \in \mathbb{R}^2$), only using N sparse sampling points, $y(\mathbf{x}_i)$, based on some optimal weights, λ_i,

$$\hat{y}(\mathbf{x}_0) = \sum_{i=1}^{N} \lambda_i y(\mathbf{x}_i). \tag{6.55}$$

For example, in ordinary kriging [85], a semivariogram is used to model the spatial variability and, given a spatial distance, h, is defined as,

$$\hat{\gamma}(h) = \frac{1}{2N(h)} \sum_{i=1}^{N(h)} (y(\mathbf{x}_i) - y(\mathbf{x}_i + h))^2. \tag{6.56}$$

This experimental semivariogram can be fitted to the model semivariogram with one of several common functions: circular, spherical, exponential, Gaussian, or linear. The weights are determined by solving

$$\sum_{j=1}^{N} \lambda_j C(\mathbf{x}_i - \mathbf{x}_j) + \mu(\mathbf{x}_0) = C(\mathbf{x}_i - \mathbf{x}_0), \text{ for } i = 1, 2, ..N, \tag{6.57}$$

where $C(\cdot)$, in this context, represents the point support covariance matrix. This matrix is related to the semivariogram, $\gamma(h) = C(0) - C(h)$ [85], and the mean square prediction error is $\sigma_e^2 = Var(y(\mathbf{x}_0) - \hat{y}(\mathbf{x}_0))$, which, for ordinary kriging, is minimized to make the estimated values $\hat{y}(\mathbf{x}_0)$ optimal. Furthermore, the estimator should be unbiased (e.g., $E[\hat{y}(\mathbf{x}_0)] = E[y(\mathbf{x}_0)]$), which requires $\sum \lambda_i = 1$ and the spatial mean to be stationary $E[y(\mathbf{x})] = \mu, \ \forall \mathbf{x} \in \Omega$.

If the kriging process is not stationary, it is considered, at best, an approximate solution to the spatial interpolation problem and incorrect at worst. A better approach could be to apply a spectral method that takes into consideration non-stationarity and higher frequencies, namely, the high frequency kriging method [44]. Consideration of temporal observations could be included as well, see quantile kriging in [60].

An enhanced version of the IDW was proposed in [62] to include an adaptive distance-decay parameter based on the density characteristics of the sampled points. Available tools, such as Kriging Assistant (KA) [63], Golden Software Surfer, or ESRI Geostatistical Analyst for ArcMap have been used in the literature before. For irregular geographical units with different sizes and shapes, the interested reader should consult [49].

A variation of the VFP technique is illustrated in [21], where a path-averaged long open path duel-comb spectroscopy is operated from a ground vehicle to a sUAS with a retro-reflector. A vertical profile is flown downwind of the source to conduct the VFP. This technique is also vary similar to VRPM.

6.1.3.2 Cylindrical Flux Plane (CFP)

A variation to the VFP is the Cylindrical Flux Plane (CFP). This method has been used with manned aircraft as it is not as easy to raster-scan a rectangular flux plane. The methodology is essentially vary similar to the VFP and can be found in the work by [74], omitted here for brevity.

6.1.3.3 Path Integrated Vertical Flux Plane (PI-VFP)

A variation of the VFP is the path integrated vertical flux plane (PI-VFP). This method utilizes a bs-TDLAS approach in that the instrument points straight down and scans or circles the emission source (see Fig. 6.6). In [42], the AVIRIS-NG manned aircraft used IMAP-DOAS technique to retrieve methane concentrations and estimated fluxes using a PI-VFP type calculation. This approach was compared with the GDT and Gaussian inverse approaches during a joint-flight campaign.

The emission rates were estimated by, $Q \approx \mathbf{u} \cdot \mathbf{n} \sum_i V_i \Delta s_i$, were V_i represents the vertically integrated concentration, and Δs_i is a path segment along the boundary. The individual measurements are integrated together (referred to as integrated methane enhancement (IME)) such that IME $= k \sum X_{CH_4}(i) \cdot S(i)$. The value X_{CH_4}

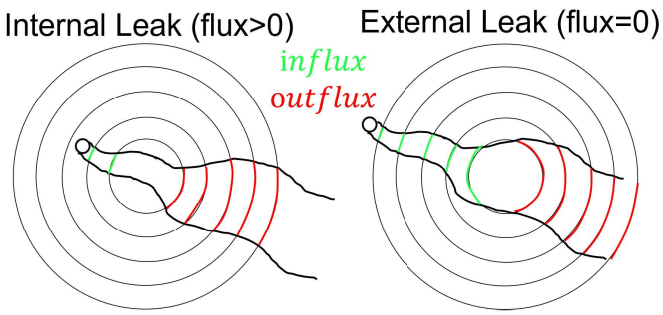

Figure 6.6 Example of the VFP-PI strategy via a UAV sensing in circular trajectories with (a) being an internal leak producing a net positive flux and (b) being an external leak producing a net zero flux. The color of the arcs are indicative of methane flux strength with green being more negative and red being more positive (see [89] for more details).

is the methane plumes that exceed the minimum threshold of 200 ppm/m and k is a conversion factor.

Using an RMLD sensor fitted to a small quadrotor UAV, a circular scanning approach can be applied to sample horizontally a site of interest. The sensor uses a bsTDLAS to measure integrated methane emissions from a known height. The resulting measurements are then combined with wind measurements to estimate the flux [43, 89],

$$Q = \oint_{\mathcal{S}} \mathbf{u} \cdot \mathbf{n}_s (y - y_b) ds, \tag{6.58}$$

where $\mathbf{n}_s$ is the normal with respect to the path of travel such that $s \in \mathcal{S}$, y is the column measured concentration and y_b is the column background concentration. This calculation encompasses a single circular loop and if the source is encapsulated, multiple passes can be used to estimate the source. For instance, given n passes,

$$\hat{Q} = \frac{1}{n} \sum Q_i. \tag{6.59}$$

In practice, the circular flight path is actually made up of line segments that are box-like. The source location was also identified by course raster scanning over the area of interest followed by a more fine flight pattern free approach combined with triangular natural neighbor interpolation. The maximum observed concentration was used for the source location.

6.1.3.4 Micrometeorological Mass Difference (MMD)

Utilizing the technique from [26], sampling the plume far enough downwind of the source, the averaged MMD can be calculated as,

$$Q = \overline{\iint U_{(x_2,x_3)} (y_{(x_2,x_3)} - y_b) dx_2 dx_3} = \int \chi(x_3) dx_3, \tag{6.60}$$

where $U_{(x_2,x_3)}$ is the normal wind speed relative to the plane. The work in [45] utilized the time-average of the line-integral of the instantaneous product of U and y in the x_2-direction. Alternatively, while using a laser fetch, an instantaneous product of a single wind measurement U and line-averaged laser concentration was used,

$$\chi \approx \Delta x_2 \overline{U_{(x_3)}(\rho_{L(x_3)} - y_b)}. \tag{6.61}$$

This method can also be used to calculate the turbulent fluxes,

$$\frac{Q_{tur}}{Q} = \frac{(Q_{\overline{U}\,\overline{y}} - Q_{\overline{Uy}})}{Q_{\overline{Uy}}}, \tag{6.62}$$

where $Q_{\overline{Uy}}$ is calculated from the flux term in (6.61) and $Q_{\overline{U}\,\overline{y}}$ in (6.63),

$$\chi \approx \Delta x_2 \overline{U_{(x_3)}}\,\overline{(y_{L(x_3)} - y_b)}. \tag{6.63}$$

This prescription of the flux does not capture the turbulent component of the horizontal flux (albeit wrong), is often necessary due to the short time-scale behavior of the wind (e.g., limitations in wind measurement devices).

6.1.3.5 Gauss Divergence Theorem (GDT)

In the paper by [20], Conley et al. they focused on the continuity equation,

$$Q_c = \left\langle \frac{\partial m}{\partial t} \right\rangle + \iiint \nabla \cdot y\mathbf{u} dV, \tag{6.64}$$

where m is the mass of the aerosol, $\langle \cdot \rangle$ is the expectation or average, $y = Y + y'$ is the concentration (comprised of an average term and a deviation term), $\mathbf{u}$ is the wind speed, and V is the volume of the area of interest. The flux divergence can be expanded as,

$$\nabla \cdot y\mathbf{u} = \mathbf{u} \cdot \nabla y + y \nabla \cdot \mathbf{u}. \tag{6.65}$$

The surface integral is taken to be a cylinder, which can be broken into several parts: the floor, the walls of the cylinder, and the top. The height of the cylinder is taken such that the emission is encapsulated with the minimum and maximum height. The resulting emission rate can be calculated as

$$Q_c = \left\langle \frac{\partial m}{\partial t} \right\rangle + \int_0^{z_{max}} \oint y' \mathbf{u}_h \cdot \hat{\mathbf{n}} dl dx_3, \tag{6.66}$$

where x_3 represents the altitude, and l the flight path. The temporal trend of the total mass ($\frac{\partial m}{\partial t}$) within the volume can be estimated from the measurements. The cylinder passes can be vertically binned and discretely summed up,

$$Q_c = \frac{\Delta m}{\Delta t} + \sum_{x_3=0}^{x_3=x_{3,max}} \Big(\sum_0^L (\rho \cdot u_n) \cdot \Delta s \Big) \cdot \Delta x_3, \tag{6.67}$$

and ρ represents the scalar air density.

6.1.3.6 Vertical Flux Planes with GLM (GLM-VFP)

In [46], a 3D grid of airborne measurements are collected across multiple landfill sites. The resulting downwind observational points are then spatially interpolated with IDW and used to calculate the total mass flux. The multiple steady state Gaussian dispersion models,

$$y(\mathbf{x}) = \frac{Q}{2\pi\sigma_{x_2}\sigma_{x_3}U}\exp\left(\frac{-x_2^2}{2\sigma_{x_2}^2}\right)\left(\frac{1}{\sqrt{2\pi\sigma_{x_3}}}\right)\exp\left[\frac{-(x_3-L)^2}{2\sigma_{x_3}^2}\right], \tag{6.68}$$

are applied to a fixed grid (50 m by 50 m), where the mixing ratios found over each individual landfill was used to calculate a model mass flux (for each site, integrated along the x_1, x_2, and x_3 directions). The experimental measurements are then used with simulation measurements and a general linear model,

$$\min_{\alpha} |MF - \sum_{i=1}^{max}(MMF_i \cdot \alpha_i)|, \tag{6.69}$$

to approximate the emission coefficient, α_i, from multiple landfill sources. The emission findings are further corroborated with a local eddy covariance tower measurement.

6.1.3.7 Vertical Radial Plume Mapping (VRPM)

The vertical radial plume mapping approach (compared with other methods in [9]), utilizes a long path TDLAS instrument from the ground. The laser is aimed at retro-reflectors, situated perpendicular and downwind of the source. The height of the retro-reflector constitutes the different radial angles where the path-integrated concentrations are combined with the normal wind component to estimate the flux (similar to VFP or MMD). An illustration of this is seen in Fig. 6.1 (see [9] for more details).

6.1.4 Image-based

In this section, we overview the imaging-based methodology for quantifying methane emissions. This typically includes techniques that sample images passively, such as TIR, MWIR, or other OGI-based instrumentation. The methods mentioned here that can quantify methane emissions are considered as quantitative optical gas imaging (QOGI).

6.1.4.1 Mid-Wave Infrared (MWIR) and Hyperspectral

In the work by [75], the detection limits of MWIR band of a hyperspectral data was explored using the Spatially-Enhanced Broadband Array Spectrograph System (SEBASS) airborne instrument. They also provided a comparison between LWIR and MWIR (see [75] for more details) using the radiative transfer model,

$$R_s = (R_T^{\uparrow} + R_S^{\uparrow}) + t\{\epsilon_s B(T_s) + (1-\epsilon_s)[\frac{R_T^{\downarrow} + R_S^{\downarrow}}{1 - S(1-\epsilon_s)}]\}, \tag{6.70}$$

where R_s is the total radiance at the sensor, $R_T^{\uparrow}$ is the upwelling emitted atmospheric path radiance, $R_T^{\downarrow}$ is the downwelling emitted atmospheric path radiance, $R_S^{\uparrow}$ is the scatter path radiance at the sensor, $R_S^{\downarrow}$ total solar radiance that reaches the surface, t is the atmospheric transmittance, ϵ_s is the surface emissivity, and $B(T_s)$ is the blackbody radiation at the surface temperature.

Other works, such as [15], have used MWIR cameras combined with two Pergam Methane Mini G lasers in pipeline leak detection. In [28], a FLIR GF320 and a RMLD were used together to make volumetric flow rate calculations in the laboratory using a data fusion approach. In [81], they utilized a thermal camera and steady state energy balance approach to estimate methane emissions from thermal anomalies in urban landfills.

6.1.4.2 Iterative Maximum a Posteriori Differential Optical Absorption Spectro-scopy (IMAP-DOAS)

The IMAP-DOAS method was applied to the AVIRIS-NG [82, 83] aircraft and measures reflected solar radiation between 0.35 μm and 2.5 μm with 5 nm spectral resolution and sampling. Using a nonlinear iterative minimization of the differences between modeled and measured radiance. The measured concentrations can be applied to the PI-VFP method to calculate fluxes [42]. Variations in this approach for retrieving methane concentrations has been seen in [38] for albedo correction and [61] anomaly-based mass balance.

6.1.5 Correlation-based

6.1.5.1 Tracer Correlation (TCM)

The tracer correlation method, or isolated source tracer ratio method, initially proposed and implemented in works by Lamb et al [58] and Czepiel et al [24], aims to quantify the emission rate of an unknown gas species by releasing a tracer gas at a known flow rate while measuring both the tracer and the unknown signals collocated downwind. This method assumes that the location of the source is known and, at the measurement location, the plume is well mixed. The elevated signal downwind also needs to typically be greater than 50 ppb. The authors report uncertainty estimates of ±15%. The general equation is given as

$$Q_m = Q_t \frac{y_m}{y_t}, \tag{6.71}$$

where Q_t is the tracer release rate, and y_m and y_t are the elevated mixing ratios of the unknown source gas and tracer gas, respectively. A comparison study between TCM and other fugitive emission quantification methods are studied in [9]. The effect of wind on accuracy of the TCM was explored for landfills using WRF model [57].

An in situ method was used to evaluate the collection efficiency of gas extraction wells based on tracer gas [56].

Variations of the quantification of TCM were explored in [64], which quantified emission rates based on the plume integration of a transect, peak height of the transect using a scatter plot to calculate the ratio (best fit line), and comparison with fitted Gaussian plume model. A landfill field comparison of methane emission models were compared to measured emissions using TCM [25]. The TCM method was also applied to quantifying emissions from dairy farms in [8].

A dual tracer method was explored in [73]. The second tracer provides for closer downwind measurements that can be refined by assessment of plume position as well as in the far-field measurements the second tracer becomes an internal standard to the measurement. A mobile version of the TCM approach was proposed in [40].

6.1.5.2 Eddy Covariance (EC)

The Eddy covariance method aims to estimate the emission flux from a footprint area given the boundary layer meteorology. Historical developments and current implementations of this method are summarized in [50]. This method generally assumes stationarity of the measured data and fully developed turbulent conditions [48]. One way it can be expressed is,

$$Q = \frac{1}{t_f - t_i} \int_{t_i}^{t_f} (y(t) - \overline{y})(w(t) - \overline{w})dt, \tag{6.72}$$

where the time-averaged concentration and vertical wind speed is $\overline{y}$ and $\overline{w}$, respectively. There are several assumptions required to make this flux calculation (for more details see [17]).

6.2 ASSESSMENT AND SUMMARY OF METHODS

In an attempt to analyze the methods covered in the previous section we decided to use the following Figure of Merit metrics,, such as: required assumptions, sample distance, survey time, complexity, average precision, average accuracy, and average cost. The required assumptions are meant to inform the practitioner so the best method can be applied to a given problem. For example, if the source location is unknown, the PSG method may not be directly applicable unless a source location estimate is supplied. The sample distance is defined as the distance from the source at which the required method is able to take measurements from. The survey time consists of the time required to make a single flux estimate. Understandably, some methods may require multiple flux estimates in order to approximate the emission source to within an acceptable error. Complexity is the measure of how difficult it is to implement any given method. In order to determine a value for complexity, a scheme was developed using figures of merit (FOM) that assigns factors and weights to the metrics (detailed in Table 6.1). Determining the values for these factors were based on loose estimates, inferred from papers found in the literature. Ranges were assigned to the metrics, as to capture variations in the factors due to either the operators or

Table 6.1 Figures of merit for defining complexity of an estimation method

FOM	(%)	Low (2.5)	Medium (5)	Med-High (7.5)	High (10)
Operator skill	30	Little	Moderate	Professional	Expert
Number of operators	25	1	2	3	3+
Equipment cost	15	<$10,000	<$50,000	<$100,000	>$100,000
Setup Time	20	<1hr	<4hr	<8hrs	8+hrs
Survey Time	10	<0.5hr	<1hr	<2hrs	2+hrs

the equipment being used, and are given in Table 6.2. For example, some setups may use more expensive equipment or more people for the same method, and as a result are reflected in the complexity metric.

Evaluating methane quantification techniques is important and much work has already gone into this topic through controlled release experiments and evaluation frameworks. Examples from controlled release facilities (CRF) consist of but are not limited to the following: In the Joint Urban 2003 study [7, 59], static sensors were distributed in an urban setting to measure the dispersion of tracer particulates; In [67], area-averaged velocity and turbulent kinetic energy profiles are derived from data collected at the Mock Urban Setting Test (MUST); Mock Urban Setting test (MUST) was also evaluated with photo-ionization detectors (PID) [12, 11]; MUST was further simulated using MISKAM 6 [32]; In [66], the WRF model was used to model wind and turbulence inside the Quick Urban & Industrial Complex (QUIC) model for comparing simulated and observed plume transport; A test plan for Jack Rabbit II was developed in [68] which aimed to improve chemical hazard modeling, produce better planning for release incidents, improve emergency response, and improve mitigation measures.

More recently, single-blind tests at the Methane Emission Technology Evaluation Center (METEC) in Fort Collins, Colorado evaluated several types of LDAQ sensing modalities as apart of the Standford/EDF Mobile Monitoring Challenge (MMC) and the Advanced Research Projects Agency-Energy (ARPA-E) MONITOR program (such as by vehicle, plane, and drone - see [70, 16] for more details). In the Standford EDF MMC it was observed that the drone based technologies performed quite well (e.g. SeekOps) with an $R^2 = 0.42$ [70]. While, the results in [70, 16] seem quite promising, there is still exists some improvements in precision that can be done. In the ARPA-E MONITOR program, 6 of the 11 participants tested their technologies at the METEC facility in [10] against 6 other industry-based participants. Due to confidentiality agreements at the time of testing, the data gathered from the 12 participants were aggregated to compare the methodologies based on measurement type (handheld, mobile and continuous monitoring). However, to the best of authors knowledge only four of the MONITOR program participants have published data regarding the METEC tests (see [92, 3, 4, 16]). In the white paper by Bridger Photonics [16], a sUAS-based approach using LiDAR-based sensor has also shown promising results even though the uncertainty is not given. In [89], a RMLD is used on a sUAS with the PI-VFP method. In contrast, [92] utilized a portable TDLAS-based instrument and the PSG method to quantify emissions. Lastly, [3] uses a dual frequency comb

spectrometer (from over one kilometer away) with the non-zero minimum bootstrap method (see [4]) and the Gaussian plume model to estimate the source rate. Examples from active operations with comparison to conventional OGI-based methods are conducted in the Alberta Methane Field Challenge (AMFC) [88, 69, 80] which aim to answer the questions: Are Leak detection and repair (LDAR) programs effective at reducing methane emissions and can new technologies provide more cost-effective leak detection compared to existing approaches?

In order to compare the performances of the each of the methods to one another, their performance metrics were garnered from different studies where the method was utilized in either a field study or a controlled release scenarios and recorded in Table 6.2. Performance values were gathered from the standard deviations of consecutive flux estimates of a singular source leak scenario. Accuracy pertains to error of the flux estimate to the known source rate. This information was limited primarily to controlled release scenarios. For each method, performances and details were separated into the broad types of sampling strategies: fixed/static, on foot, mounted on a vehicle, mounted on an aircraft, and mounted on a sUAS. This prevents convolution of performance values between, for example, long aircraft sampling flights at far distances and short sampling flights near the source via sUAS.

After analyzing the quantification methods we can separate methods based on whether they have used sUAS or not. In this manuscript we observed that the sUAS-based methods consist of: Near-field Gaussian plume inverse (NGI), vertical flux plane (VFP), and the path-integrated vertical flux plane (PI-VFP). The non-sUAS-based methods consist of: backwards Lagragian Stochastic (bLS), point source Gaussian (PSG), recursive Bayesian point source Gaussian (PSG-RB), conditionally sampled point source Gaussian (PSG-CS), micrometeorological mass difference (MMD), Gauss divergence theorem (GDT), VFP, PI-VFP, cylindrical flux plane (CFP), general linear model verticl flux plane (GLM-VFP), vertical radial plume mapping (VRPM), quantitative optical gas imaging (QOGI), tracer correlation method (TCM), and Eddy covariance (EC). When comparing their performances in Table 6.2, it can be seen that, when categorizing by means of mobility (i.e. fixed, on-foot, etc.), methods using static sensors show a trend of having higher complexity values while UAV-based methods display generally lower complexity values. For a subset of the methods, the survey times, sample distances, and average accuracies can be seen in Fig. 6.7. This subset was specifically displayed for these methods had both upper and lower bounds for survey times and sample distances along with accuracy data which allowed for the plotting of these quantities for each method in the form of ellipses on a log-log plot. When analyzing this plot, it can be seen that the sUAS-based methods are generally lower in sample distances and survey times as opposed to manned aircraft-based methods (being the one of the highest in both). The bLS and TCM methods are shown to have the best average accuracy with several sUAS and mobile methods close in accuracy. The long sample times of bLS method are due to the values reported in [79], and it is possible that these values don't reflect typical bLS sample times. The advantages and disadvantages of each of the methods can be seen in Table 6.3 along with what typical application fields that they were applied in.

The final ranking of the methods depends heavily on the desired application,

Table 6.2 Summary of methods and their assumptions, operational details, complexity, cost, average precision, and average accuracy are generalized over implementations found in the literature. The average precision and accuracy are given as unitless values, normalized by the true source rate (estimated source rate). (measured using [1]fixed, [2]foot, [3]vehicle, [4]manned aircraft, or [5]UAV; cost with $ ≤$10,000, $$ ≤$50,000, $$$ ≤$100,000, $$$$ ≥$100,000; (·) represents precision normalized on estimated source rate average complexity.

Method	**Assumptions**	**Sample Distance**	**Survey Time**	**Complexity** (1-10)	**Avg Precision**	**Avg Accuracy**	**Avg Cost**
bLS	x_s, horizontally uniform surface source atmosphere in horizontal equilibrium	20-441m[1]	15min-4days[1]	3.8-8.5[1]	±0.16-0.36[1] (±0.07-0.85)[1]	±0.02-0.30[1]	$-$$$[1]
PSG	x_s, steady state source rate, point source, plume evolution via ground-level Gaussian dispersion with no obstructions	441m[1] 18-500m[3] 50m[5]	4days[1] 37-58min[3] 7.22-20min[5]	4.5-8[1] 3.6-6.1[3] 3.3-5.5[5]	(±0.30)[1], ±0.20-0.67[3] (±0.19-0.47)[3] ±0.31[5]	±0.0022-0.43[3] ±0.50[5]	$$-$$$[3]
PSG-RB	*PSG assumptions*, vertical eddy diffusivity and wind speed approximated by power law scheme	20-200m[3]	6min[3]	3.6-6.4[3]	—	±0[3]	$$-$$$
PSG-CS	*PSG assumptions*, continuous source emission, constant wind speed, vertical eddy diffusivity and wind speed approximated by power law	18-106m[3]	20min[3]	3.6-5.9[3]	±0.20-0.67[3] (±0.19-0.47)[3]	±0.02-0.26[3]	$$-$$$[3]
NGI	constant source rate , σ_x and σ_y linear functions of distance to source	50-82.25m[5]	7.35-29.62min[5]	3.3-5.5[5]	±0.21-0.58[5] (±0.06-0.53)[5]	±0.11-0.13[5]	$-$$[5]
MMD	x_s	12-27m[1]	15min[1]	4.5-8.1[1]	±0.06[1]	±0.10[1]	$$$-$$$$[1]
GDT	near to no meandering, steady state source rate	3-8km[4]	1hr[4]	5.5-7.8[4]	±0.07[4] (±0.08)[4]	±0.13[4]	$$$-$$$$[4]
VFP	*GDT assumptions*	4.875-10km[4] 19.08-510m[5]	1.5-4.5hr[4] 20-30min[5]	5.8-8.3[4] 3.3-5.5[5]	(±0.30-0.53)[4] ±0.17-0.0.37[5] (±0.013-0.62)[5]	±0.10-0.50[4] ±0.03-0.50[5]	$$$-$$$$[4] $-$$[5]
PI-VFP	*GDT assumptions*	3km[4] 0-6.77m[5]	20-30min[4] 15-20min[5]	5.3-7.5[4] 3.3-5.5[5]	(±0.34-0.58)[4] ±0.82[5]	±0.27-52[5]	$$$-$$$$[4] $-$$[5]
CFP	*GDT assumptions*	3-17.84km[4]	1hr[4]	5.5-7.8[4]	—	—	$$$-$$$$[4]
GLM-VFP	*GDT assumptions*	0.4-2.2km[4]	2.5hr[4]	6-8.3[4]	(±0.21)[4]	—	$$$-$$$[4]
VRPM	*GDT assumptions*	10-100m[1]	1hr[1]	7.1-8.6[1]	±0.18-0.21[1] (±0.21-0.33)[1]	±0.05-0.43[1]	$-$$$[1]
QOGI	temperature and pressure of gas at leak location are the same, gas plume length in direction of optical path is small	30m[1]	1min[1]	3-6.3[1]	±0.01-0.02[1] (±0.02-0.03)[1]	±0.20-0.24[1]	$-$$$[1]
TCM	leak plume and tracer plume are well mixed	100-3546m[3]	0.5-2hr[3]	4.6-7.6[3]	±0.06-0.24[3] (±0.06-0.74)[3]	±0.0056-0.17[3]	$$-$$$[3]
EC	stationarity, fully developed turbulent conditions	25-228m[1]	—	4.5-7.8[1]	(±0.08)[1]	—	$-$$$[1]

which also depends on factors such as sample distance, sample time, and desired accuracy. For that reason, it is difficult to rank the methods in general. Thus, we provide a ranking of the methods in terms of complexity (outlined in Table 6.1) with highlights from the precision and cost in Fig. 6.8. The results indicate that the simplest methods, in terms of complexity, are the sUAS-based NGI[5] and VFP[5] as well as fixed QOGI[1]. The most complex methods include bLS[1] and manned aircraft-based approaches. In terms of precision, bLS[1], NGI[5], GDT[4], VFP[5], QOGI[1], TCM[3], and EC[1] tend to be the best. Thus, for sUAS-based methods, NGI[5] and VFP[5], are the most promising approaches. Additionally, the GDT[4], TCM[3], and EC[1] approaches can be treated as candidate methods for future implementation using sUAS.

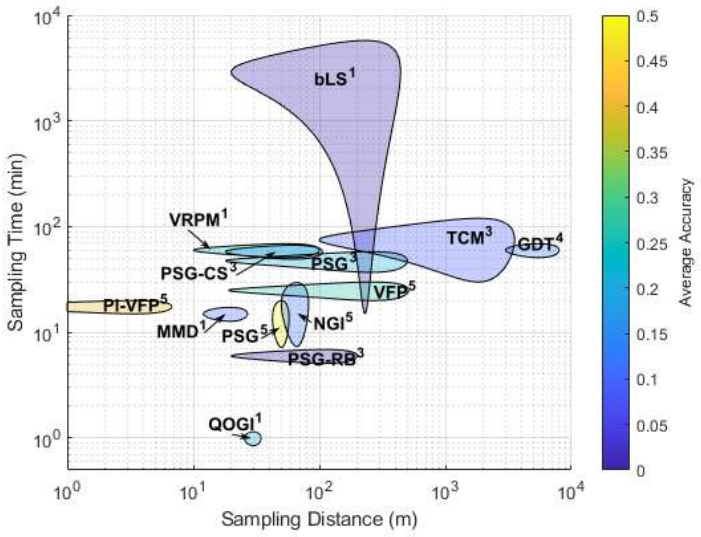

Figure 6.7 Diagram of summary of methods (based on Table 6.2) showing relationship between typical survey time versus sample distance and there associated normalized accuracy, where lower values represent more accurate measurements. (measured using [1]fixed, [2]foot, [3]vehicle, [4]manned aircraft, or [5]UAV)

6.3 CHAPTER SUMMARY

In this chapter, we examined several key emission source quantification (ESQ) methods that utilize simulation-, mass-balance-, correlation-, and image-based approaches. Within the methods examined, we noted several sUAS-based approaches. This includes methods that utilize optimization and mass-balance principals, such as the near-field Gaussian plume inversion (NGI) and the mass-balance vertical flux plane (VFP) – also cylindrical flux plane (CFP). While, some of the methods utilized mobile vehicles, it is possible that methods such as the recursive Bayesian point source Gaussian (PSG-RB) or tracer correlation method (TCM) can be extended to sUAS-based too.

An analysis and summary of the all methods were conducted to showcase the

Table 6.3 Summary of method advantages and disadvantages along with fields of application

Method	**Application**	**Advantages**	**Disadvantages**
bLS	General, Oil and Gas, Agriculture	able to quantify area source and point source emissions	sensor is fixed, multiple measurements, negatively impacted by obstacles
PSG	Biogas, Oil and Gas	No tracer required	Negatively impacted by obstacles and low wind speeds due to plume advection, mobile sensors limited to roads
PSG-RB	Oil and Gas	No tracer required, accurate source quantification in open environments	*PSG limitations*
PSG-CS	Oil and Gas	No tracer required	*PSG limitations*
NGI	General, Oil and Gas	assumes near-field plume turbulence and wind meandering	near-field (100m), prop-wash interference if unaccounted for
MMD	Agriculture	able to give instantaneous flux estimates	fixed sensors
GDT	Regional	capable of giving emission quantifications of large areas	Sample around closed volume typically large areas, unable to capture instantaneous methane flux
VFP	General, Oil and Gas, Landfill	does not require exact source location, ease of mobility	stable atmospheric conditions, unable to capture instantaneous methane flux
PI-VFP	General, Oil and Gas	*VFP advantages*	*VFP limitations*
CFP	General, Urban	capable of giving emission quantifications of large areas	*GDT limitations*
GLM-VFP	Landfill	*VFP advantages*	*VFP limitations*
VRPM	Landfill	able to give instantaneous flux estimates	fixed sensors
QOGI	Biogas	able to give instantaneous flux estimates	gas velocity determined via gas camera - velocity component parallel to image plane, can be difficult to process images
TCM	General, Oil and Gas, Landfill, Urban	does not rely on meteorological measurements	mobile sensors limited to roads, application difficulty due to outside methane source interference
EC	General, Oil and Gas	can capture emission variations due to long time series	fixed sensor(s), stable atmospheric conditions, sensitive to time of day, typically requires long sampling times

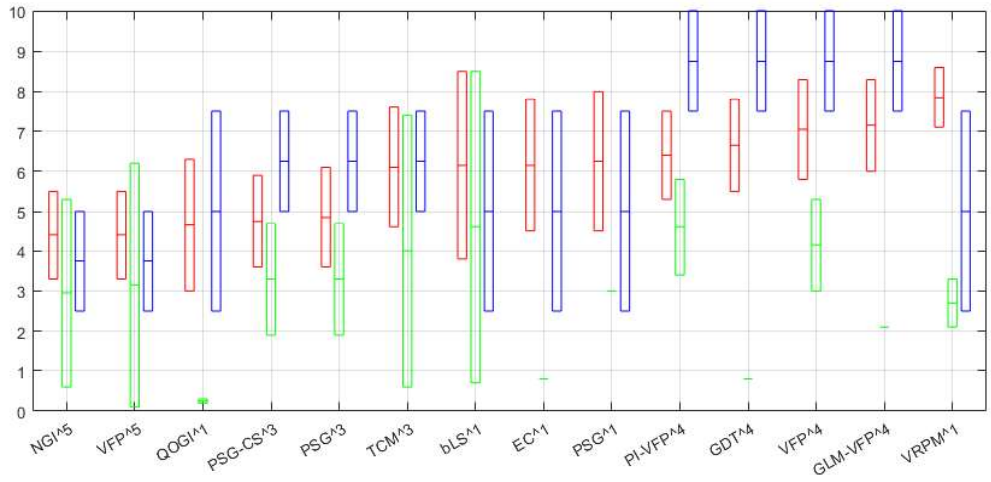

Figure 6.8 Diagram of the complexity ranking of the methods (based on Table 6.1), showing the relationship between the method complexity (red), precision (green), and cost (blue). The precision is normalized on the source estimate multiplied by 10 and the cost is ranked from 0 to 10. (measured using [1]fixed, [2]foot, [3]vehicle, [4]manned aircraft, or [5]UAV)

complexity, cost and accuracy (or variance if not available). These insights were displayed in Section 6.2's Tables and Figures to help give practitioners a large scale overview of the required sample distance, sample time, accuracy, cost and complexity. While, these metrics are generalized to some extent, the usefulness is in the selection of the appropriate method and mode of sensing for your desired application. In this context, the sUAS-based approaches tended to be the simplest (in regards to comlpexity) compared to the other methods examined. Additionally, of the sUAS-based approaches, the mass balanced-based and NGI methods were more dominant. It should be noted that the Sequential Bayesian Markov Chain Monte Carlo approach in [55] shows promise in terms of source term estimation but needs further evaluation for applications in Oil & Gas (ONG). This is in part due to operator concerns of intrinsically safe devices being near ONG equipment, as well as, some operators do not allow flights over the equipment [88, 80].

Bibliography

[1] Adil Shah. Supplement to A Near-Field Gaussian Plume Inversion Flux Quantification Method, Suitable For Unmanned Aerial Vehicle Sampling. *Atmosphere*, 2020.

[2] John D Albertson, Tierney Harvey, Greg Foderaro, Pingping Zhu, Xiaochi Zhou, Silvia Ferrari, M Shahrooz Amin, Mark Modrak, Halley Brantley, and Eben D Thoma. A mobile sensing approach for regional surveillance of fugitive methane emissions in oil and gas production. *Environmental Science & Technology*, 50(5):2487–2497, 2016.

[3] Caroline B Alden, Sean C Coburn, Robert J Wright, Esther Baumann, Kevin Cossel, Edgar Perez, Eli Hoenig, Kuldeep Prasad, Ian Coddington, and Gregory B Rieker. Single-blind quantification of natural gas leaks from 1 km distance using frequency combs. *Environmental science & technology*, 53(5):2908–2917, 2019.

[4] Caroline B Alden, Subhomoy Ghosh, Sean Coburn, Colm Sweeney, Anna Karion, Robert Wright, Ian Coddington, Gregory B Rieker, and Kuldeep Prasad. Bootstrap inversion technique for atmospheric trace gas source detection and quantification using long open-path laser measurements. *Atmospheric Measurement Techniques*, 11(3):1565–1582, 2018.

[5] David Allen, Shannon Stokes, Erin Tullos, Brendan Smith, Scott Herndon, and Bradley Flowers. Field trial of methane emission quantification technologies. In *Proc. of the SPE Annual Technical Conference and Exhibition*. OnePetro, 2020.

[6] Grant Allen, Peter Hollingsworth, Khristopher Kabbabe, Joseph R Pitt, Mohammed I Mead, Samuel Illingworth, Gareth Roberts, Mark Bourn, Dudley E Shallcross, and Carl J Percival. The development and trial of an unmanned aerial system for the measurement of methane flux from landfill and greenhouse gas emission hotspots. *Waste Management*, 87:883–892, 2019.

[7] K Jerry Allwine and Julia E Flaherty. Joint urban 2003: Study overview and instrument locations. Technical report, Pacific Northwest National Lab.(PNNL), Richland, WA (United States), 2006.

[8] C Arndt, AB Leytem, AN Hristov, D Zavala-Araiza, JP Cativiela, S Conley, C Daube, Ian Faloona, and SC Herndon. Short-term methane emissions from 2 dairy farms in california estimated by different measurement techniques and us

environmental protection agency inventory methodology: A case study. *Journal of Dairy Science*, 101(12):11461–11479, 2018.

[9] Antoine Babilotte. Field comparison of methods for assessment of methane fugitive emissions from landfills. *Environmental Research and Education Foundation (EREF)*, 2011.

[10] Clay S Bell, Timothy Vaughn, Daniel Zimmerle, Detlev Helmig, and Brian Lamb. Evaluation of next generation emission measurement technologies under repeatable test protocols. *Elementa: Science of the Anthropocene*, 8, 2020.

[11] C. A. Biltoft and E Yee. Overview of the Mock Urban Setting Test (MUST) C.A. *Engineering*, 2001.

[12] CHRISTOPHER A Biltoft. Customer report for mock urban setting test. *DPG Document*, (8-CO):160–000, 2001.

[13] M Bourn, G Allen, P Hollingsworth, K Kababbe, P I Williams, H Ricketts, J R Pitt, and A Shah. The development of an unmanned aerial system for the measurement of methane emissions from landfill. *Sixteenth International Waste Management and Landfill Symposium*, (October 2017), 2018.

[14] Halley L Brantley, Eben D Thoma, William C Squier, Birnur B Guven, and David Lyon. Assessment of methane emissions from oil and gas production pads using mobile measurements. *Environmental Science & Technology*, 48(24):14508–14515, 2014.

[15] Timo Rolf Bretschneider and Karan Shetti. UAV-based gas pipeline leak detection. *35th Asian Conference on Remote Sensing 2014, ACRS 2014: Sensing for Reintegration of Societies*, (April), 2014.

[16] Bridger Photonics. Gas mapping lidar™ METEC round 1 results.

[17] George Burba. *Eddy covariance method for scientific, industrial, agricultural and regulatory applications: A field book on measuring ecosystem gas exchange and areal emission rates*. LI-Cor Biosciences, 2013.

[18] Maria Obiminda L Cambaliza, Jean E Bogner, Roger B Green, Paul B Shepson, Tierney A Harvey, Kurt A Spokas, Brian H Stirm, Margaret Corcoran, Detlev Helmig, and Armin Wisthaler. Field measurements and modeling to resolve m^2 to km^2 ch_4 emissions for a complex urban source: An indiana landfill study. *Elementa: Science of the Anthropocene*, 5, 2017.

[19] MOL Cambaliza, PB Shepson, DR Caulton, B Stirm, D Samarov, KR Gurney, J Turnbull, KJ Davis, A Possolo, A Karion, et al. Assessment of uncertainties of an aircraft-based mass balance approach for quantifying urban greenhouse gas emissions. *Atmospheric Chemistry and Physics*, 14(17):9029–9050, 2014.

[20] Stephen Conley, Ian Faloona, Shobhit Mehrotra, Maxime Suard, Donald H Lenschow, Colm Sweeney, Scott Herndon, Stefan Schwietzke, Gabrielle Pétron, Justin Pifer, et al. Application of gauss's theorem to quantify localized surface emissions from airborne measurements of wind and trace gases. *Atmospheric Measurement Techniques*, 10(9):3345–3358, 2017.

[21] Kevin C. Cossel, Eleanor M. Waxman, Eli Hoenig, Michael Cermak, Chris Choate, Daniel Hesselius, Ian Coddington, and Nathan R. Newbury. Micrometeorological flux measurements using spatially- scanned open-path dual-comb spectroscopy. *Optical Sensors and Sensing Congress*, 2020(c):EM3C.2, 2021.

[22] Noel Cressie. Kriging nonstationary data. *Journal of the American Statistical Association*, 81(395):625–634, 1986.

[23] Yu Yan Cui, Jerome Brioude, Stuart A McKeen, Wayne M Angevine, Si-Wan Kim, Gregory J Frost, Ravan Ahmadov, Jeff Peischl, Nicolas Bousserez, Zhen Liu, et al. Top-down estimate of methane emissions in California using a mesoscale inverse modeling technique: The South Coast Air Basin. *Journal of Geophysical Research: Atmospheres*, 120(13):6698–6711, 2015.

[24] PM Czepiel, B Mosher, RC Harriss, JH Shorter, JB McManus, CE Kolb, E Allwine, and BK Lamb. Landfill methane emissions measured by enclosure and atmospheric tracer methods. *Journal of Geophysical Research: Atmospheres*, 101(D11):16711–16719, 1996.

[25] Florentino B De la Cruz, Roger B Green, Gary R Hater, Jeffrey P Chanton, Eben D Thoma, Tierney A Harvey, and Morton A Barlaz. Comparison of field measurements to methane emissions models at a new landfill. *Environmental Science & Technology*, 50(17):9432–9441, 2016.

[26] OT Denmead, LA Harper, JR Freney, DWT Griffith, R Leuning, and RR Sharpe. A mass balance method for non-intrusive measurements of surface-air trace gas exchange. *Atmospheric Environment*, 32(21):3679–3688, 1998.

[27] John D'Errico. fminsearchbnd, fminsearchcon, Feb 2022.

[28] Sören Dierks and Andreas Kroll. Quantification of methane gas leakages using remote sensing and sensor data fusion. In *Proc. of the 2017 IEEE Sensors Applications Symposium (SAS)*, pages 1–6. IEEE, 2017.

[29] Richard M Eckman. Re-examination of empirically derived formulas for horizontal diffusion from surface sources. *Atmospheric Environment*, 28(2):265–272, 1994.

[30] Rachel Edie, Anna M Robertson, Robert A Field, Jeffrey Soltis, Dustin A Snare, Daniel Zimmerle, Clay S Bell, Timothy L Vaughn, and Shane M Murphy. Constraining the accuracy of flux estimates using OTM 33A. *Atmospheric Measurement Techniques*, 13(1):341–353, 2020.

[31] Rachel Edie, Anna M Robertson, Jeffrey Soltis, Robert A Field, Dustin Snare, Matthew D Burkhart, and Shane M Murphy. Off-site flux estimates of volatile organic compounds from oil and gas production facilities using fast-response instrumentation. *Environmental Science & Technology*, 54(3):1385–1394, 2019.

[32] Joachim Eichhorn and Márton Balczó. Flow and dispersal simulations of the mock urban setting test. *Hrvatski meteorološki časopis*, 43(43/1):67–72, 2008.

[33] EPA. Draft Other Test Method 33A: Geospatial measurement of air pollution, remote emissions quantification - direct assessment (GMAP-REQ-DA). *Environmental Protection Agency (EPA)*, 2014. https://www3.epa.gov/ttnemc01/prelim/otm33a.pdf.

[34] Thomas K Flesch, Sean M McGinn, Deli Chen, John D Wilson, and Raymond L Desjardins. Data filtering for inverse dispersion emission calculations. *Agricultural and Forest Meteorology*, 198:1–6, 2014.

[35] Thomas K Flesch, John D Wilson, and Eugene Yee. Backward-time lagrangian stochastic dispersion models and their application to estimate gaseous emissions. *Journal of Applied Meteorology and Climatology*, 34(6):1320–1332, 1995.

[36] TK Flesch, JD Wilson, and LA Harper. Deducing ground-to-air emissions from observed trace gas concentrations: a field trial with wind disturbance. *Journal of Applied Meteorology*, 44(4):475–484, 2005.

[37] TK Flesch, JD Wilson, LA Harper, BP Crenna, and RR Sharpe. Deducing ground-to-air emissions from observed trace gas concentrations: a field trial. *Journal of Applied Meteorology*, 43(3):487–502, 2004.

[38] Markus D Foote, Philip E Dennison, Andrew K Thorpe, David R Thompson, Siraput Jongaramrungruang, Christian Frankenberg, and Sarang C Joshi. Fast and accurate retrieval of methane concentration from imaging spectrometer data using sparsity prior. *IEEE Transactions on Geoscience and Remote Sensing*, 58(9):6480–6492, 2020.

[39] Tierney A Foster-Wittig, Eben D Thoma, and John D Albertson. Estimation of point source fugitive emission rates from a single sensor time series: A conditionally-sampled gaussian plume reconstruction. *Atmospheric Environment*, 115:101–109, 2015.

[40] Tierney A Foster-Wittig, Eben D Thoma, Roger B Green, Gary R Hater, Nathan D Swan, and Jeffrey P Chanton. Development of a mobile tracer correlation method for assessment of air emissions from landfills and other area sources. *Atmospheric Environment*, 102:323–330, 2015.

[41] James L France, Prudence Bateson, Pamela Dominutti, Grant Allen, Stephen Andrews, Stephane Bauguitte, Max Coleman, Tom Lachlan-Cope, Rebecca E Fisher, Langwen Huang, et al. Facility level measurement of offshore oil and

gas installations from a medium-sized airborne platform: method development for quantification and source identification of methane emissions. *Atmospheric Measurement Techniques*, 14(1):71–88, 2021.

[42] Christian Frankenberg, Andrew K Thorpe, David R Thompson, Glynn Hulley, Eric Adam Kort, Nick Vance, Jakob Borchardt, Thomas Krings, Konstantin Gerilowski, Colm Sweeney, et al. Airborne methane remote measurements reveal heavy-tail flux distribution in four corners region. *Proc. of the National Academy of Sciences*, 113(35):9734–9739, 2016.

[43] Michael B. Frish. Monitoring fugitive methane emissions utilizing advanced small unmanned aerial sensor technology. 2016. http://www.psicorp.com/sites/psicorp.com/files/articles/SR-2018-3.pdf.

[44] Montserrat Fuentes. A high frequency kriging approach for non-stationary environmental processes. *Environmetrics: The official journal of the International Environmetrics Society*, 12(5):469–483, 2001.

[45] Zhiling Gao, Raymond L Desjardins, and Thomas K Flesch. Comparison of a simplified micrometeorological mass difference technique and an inverse dispersion technique for estimating methane emissions from small area sources. *Agricultural and Forest Meteorology*, 149(5):891–898, 2009.

[46] D. Gasbarra, P. Toscano, D. Famulari, S. Finardi, P. Di Tommasi, A. Zaldei, P. Carlucci, E. Magliulo, and B. Gioli. Locating and quantifying multiple landfills methane emissions using aircraft data. *Environmental Pollution*, 254:112987, 2019.

[47] Jake R Gemerek, Silvia Ferrari, and John D Albertson. Fugitive gas emission rate estimation using multiple heterogeneous mobile sensors. In *Proc. of the 2017 ISOCS/IEEE International Symposium on Olfaction and Electronic Nose (ISOEN)*, pages 1–3. IEEE, 2017.

[48] Mathias Göckede, Corinna Rebmann, and Thomas Foken. A combination of quality assessment tools for eddy covariance measurements with footprint modelling for the characterisation of complex sites. *Agricultural and Forest Meteorology*, 127(3-4):175–188, 2004.

[49] Pierre Goovaerts. Kriging and semivariogram deconvolution in the presence of irregular geographical units. *Mathematical Geosciences*, 40(1):101–128, 2008.

[50] Bruce B Hicks and Dennis D Baldocchi. Measurement of fluxes over land: Capabilities, origins, and remaining challenges. *Boundary-Layer Meteorology*, 177:365–394, 2020.

[51] Derek Hollenbeck and YangQuan Chen. Characterization of ground-to-air emissions with sUAS using a digital twin framework. In *Proc. of the 2020 International Conference on Unmanned Aircraft Systems (ICUAS)*, pages 1162–1166. IEEE, 2020.

[52] Derek Hollenbeck, Kristen Manies, YangQuan Chen, Dennis Baldocchi, Eugenie Euskirchen, and Lance Christensen. Evaluating a uav-based mobile sensing system designed to quantify ecosystem-based methane. *Earth and Space Science Open Archive*, page 15, 2021.

[53] Nicholas S Holmes and Lidia Morawska. A review of dispersion modelling and its application to the dispersion of particles: an overview of different dispersion models available. *Atmospheric Environment*, 40(30):5902–5928, 2006.

[54] C Hunter. A recommended Pasquill-Gifford stability classification method for safety basis atmospheric dispersion modeling at SRS. Technical report, Savannah River Site (SRS), 2012.

[55] Michael Hutchinson, Cunjia Liu, and Wen-Hua Chen. Source term estimation of a hazardous airborne release using an unmanned aerial vehicle. *Journal of Field Robotics*, 36(4):797–817, 2019.

[56] Paul Imhoff, Ramin Yazdani, Byunghyun Han, Changen Mei, and Don Augenstein. Quantifying capture efficiency of gas collection wells with gas tracers. *Waste Management*, 43:319–327, 2015.

[57] Paul T Imhoff and Fotini K Chow. Assessing Accuracy of Tracer Dilution Measurements of Methane Emissions from Landfills with Wind Modeling Research Proposal Assessing Accuracy of Tracer Dilution Measurements of Methane Emissions from Landfills with Wind Modeling. 2014.

[58] Brian K Lamb, J Barry McManus, Joanne H Shorter, Charles E Kolb, Byard Mosher, Robert C Harriss, Eugene Allwine, Denise Blaha, Touche Howard, Alex Guenther, et al. Development of atmospheric tracer methods to measure methane emissions from natural gas facilities and urban areas. *Environmental Science & Technology*, 29(6):1468–1479, 1995.

[59] MJ Leach. Final report for the joint urban 2003 atmospheric dispersion study in Oklahoma City: Lawrence livermore national laboratory participation. Technical report, Lawrence Livermore National Lab.(LLNL), Livermore, CA (United States), 2005.

[60] Henning Lebrenz and András Bárdossy. Geostatistical interpolation by quantile kriging. *Hydrology and Earth System Sciences*, 23(3):1633–1648, 2019.

[61] Ira Leifer, Christopher Melton, Marc L Fischer, Matthew Fladeland, Jason Frash, Warren Gore, Laura T Iraci, Josette E Marrero, Ju-Mee Ryoo, Tomoaki Tanaka, et al. Atmospheric characterization through fused mobile airborne and surface in situ surveys: methane emissions quantification from a producing oil field. *Atmospheric Measurement Techniques*, 11(3):1689–1705, 2018.

[62] George Y Lu and David W Wong. An adaptive inverse-distance weighting spatial interpolation technique. *Computers & Geosciences*, 34(9):1044–1055, 2008.

[63] Alessandro Mazzella and Antonio Mazzella. The importance of the model choice for experimental semivariogram modeling and its consequence in evaluation process. *Journal of Engineering*, 2013, 2013.

[64] Jacob G MØnster, Jerker Samuelsson, Peter Kjeldsen, Chris W Rella, and Charlotte Scheutz. Quantifying methane emission from fugitive sources by combining tracer release and downwind measurements–a sensitivity analysis based on multiple field surveys. *Waste Management*, 34(8):1416–1428, 2014.

[65] Randulph P Morales, Jonas Ravelid, Killian P Brennan, Béla Tuzson, Lukas Emmenegger, and Dominik Brunner. Estimating local methane sources from drone-based laser spectrometer measurements by mass-balance method. In *EGU General Assembly Conference Abstracts*, page 14778, 2020.

[66] Matthew A Nelson, Michael J Brown, Scot A Halverson, Paul E Bieringer, Andrew Annunzio, George Bieberbach, and Scott Meech. A case study of the weather research and forecasting model applied to the joint urban 2003 tracer field experiment. part 2: Gas tracer dispersion. *Boundary-Layer Meteorology*, 161(3):461–490, 2016.

[67] Matthew A Nelson, MJ Brown, ER Pardyjak, and JC Klewicki. Area-averaged profiles over the mock urban setting test array. Technical report, Los Alamos National Laboratory, 2004.

[68] Damon K Nicholson, Allison Hedrick, Petr Serguievski, and Allyssa A Martinez. Detailed test plan for Jack Rabbit (JR) II. Technical report, West Desert Test Center Dugway Proving Ground UT, 2015.

[69] Arvind P Ravikumar, Brenna Barlow, Jiayang Wang, and Devyani Singh. Results from the Alberta methane measurement campaigns: New insights into oil and gas methane mitigation policy. In *AGU Fall Meeting Abstracts*, volume 2019, pages A41D–08, 2019.

[70] Arvind P Ravikumar, Sindhu Sreedhara, Jingfan Wang, Jacob Englander, Daniel Roda-Stuart, Clay Bell, Daniel Zimmerle, David Lyon, Isabel Mogstad, Ben Ratner, et al. Single-blind inter-comparison of methane detection technologies–results from the stanford/edf mobile monitoring challenge. *Elementa: Science of the Anthropocene*, 7, 2019.

[71] Maximilian Reuter, Heinrich Bovensmann, Michael Buchwitz, Jakob Borchardt, Sven Krautwurst, Konstantin Gerilowski, Matthias Lindauer, Dagmar Kubistin, and John P. Burrows. Development of a small unmanned aircraft system to derive CO_2 emissions of anthropogenic point sources. *Atmospheric Measurement Techniques*, 14(1):153–172, 2021.

[72] Kyoung S Ro, Melvin H Johnson, Kenneth C Stone, Patrick G Hunt, Thomas Flesch, and Richard W Todd. Measuring gas emissions from animal waste lagoons with an inverse-dispersion technique. *Atmospheric Environment*, 66:101–106, 2013.

[73] JR Roscioli, TI Yacovitch, C Floerchinger, AL Mitchell, DS Tkacik, R Subramanian, DM Martinez, TL Vaughn, L Williams, D Zimmerle, et al. Measurements of methane emissions from natural gas gathering facilities and processing plants: measurement methods. *Atmospheric Measurement Techniques*, 8(5):2017–2035, 2015.

[74] Ju Mee Ryoo, Laura T. Iraci, Tomoaki Tanaka, Josette E. Marrero, Emma L. Yates, Inez Fung, Anna M. Michalak, Jovan Tadić, Warren Gore, T. Paul Bui, Jonathan M. Dean-Day, and Cecilia S. Chang. Quantification of CO_2 and CH_4 emissions over Sacramento, California, based on divergence theorem using aircraft measurements. *Atmospheric Measurement Techniques*, 12(5):2949–2966, 2019.

[75] Rebecca Del Papa Moreira Scafutto and Carlos Roberto de Souza Filho. Detection of methane plumes using airborne midwave infrared (3-5 μm) hyperspectral data. *Remote Sensing*, 10(8):1–16, 2018.

[76] Adil Shah, Grant Allen, Joseph R Pitt, Hugo Ricketts, Paul I Williams, Jonathan Helmore, Andrew Finlayson, Rod Robinson, Khristopher Kabbabe, Peter Hollingsworth, et al. A near-field gaussian plume inversion flux quantification method, applied to unmanned aerial vehicle sampling. *Atmosphere*, 10(7):396, 2019.

[77] Adil Shah, Grant Allen, Hugo Ricketts, Joseph Pitt, and Paul Williams. Methane flux quantification from lactating cattle using unmanned aerial vehicles. *EGU General Assembly*, 20:7655, 2018.

[78] Adil A Shah. Methane Flux Quantification Using Unmanned Aerial Vehicles. *Diss., University of Manchester*, 2020.

[79] Jacob T Shaw, Grant Allen, Joseph Pitt, Adil Shah, Shona Wilde, Laurence Stamford, Zhaoyang Fan, Hugo Ricketts, Paul I Williams, Prudence Bateson, et al. Methane flux from flowback operations at a shale gas site. *Journal of the Air & Waste Management Association*, 70(12):1324–1339, 2020.

[80] Devyani Singh, Brenna Barlow, Chris Hugenholtz, Wes Funk, Cooper Robinson, and Arvind P Ravikumar. Field performance of new methane detection technologies: Results from the Alberta Methane Field Challenge. 2021.

[81] Giovanni Tanda, Marco Balsi, Paolo Fallavollita, and Valter Chiarabini. A UAV-based thermal-imaging approach for the monitoring of urban landfills. *Inventions*, 5(4):1–13, 2020.

[82] AK Thorpe, C Frankenberg, and DA Roberts. Retrieval techniques for airborne imaging of methane concentrations using high spatial and moderate spectral resolution: Application to aviris. *Atmospheric Measurement Techniques*, 7(2):491–506, 2014.

[83] Andrew K Thorpe, Christian Frankenberg, David R Thompson, Riley M Duren, Andrew D Aubrey, Brian D Bue, Robert O Green, Konstantin Gerilowski, Thomas Krings, Jakob Borchardt, et al. Airborne doas retrievals of methane, carbon dioxide, and water vapor concentrations at high spatial resolution: application to aviris-ng. *Atmospheric Measuremnt Techniques*, 10(10), 2017.

[84] AP Van Ulden. Simple estimates for vertical diffusion from sources near the ground. *Atmospheric Environment*, 12(11):2125–2129, 1978.

[85] Hans Wackernagel. Ordinary Kriging. In *Multivariate Geostatistics*, pages 79–88. Springer, 2003.

[86] M Whiticar, L Christensen, C Salas, and P Reece. GHGMap: novel approach for aerial measurements of greenhouse gas emissions British Columbia. *Geoscience BC Summary of Activities 2017: Energy, Geoscience BC, Report 2018-4*, pages 1–10, 2018.

[87] M Whiticar, L Christensen, C Salas, and P Reece. Ghgmap: Detection of fugitive methane leaks from natural gas pipelines British Columbia and Alberta. *Geoscience BC Summary of Activities 2018: Energy and Water, Geoscience BC, Report 2019-2*, pages 67–76, 2019.

[88] M Whiticar, D Hollenbeck, B Billwiller, C Salas, and L.E Christensen. Application of the bc GHGMapper™ platform for the Alberta Methane Field Challenge (AMFC). *Geoscience BC Summary of Activities 2019: Energy and Water, Geoscience BC, Report 2020-02*, pages 87–102, 2020.

[89] Shuting Yang, Robert W Talbot, Michael B Frish, Levi M Golston, Nicholas F Aubut, Mark A Zondlo, Christopher Gretencord, and James McSpiritt. Natural gas fugitive leak detection using an unmanned aerial vehicle: Measurement system description and mass balance approach. *Atmosphere*, 9(10):383, 2018.

[90] Eugene Yee. Probability theory as logic: data assimilation for multiple source reconstruction. *Pure and Applied Geophysics*, 169(3):499–517, 2012.

[91] Eugene Yee and Thomas K Flesch. Inference of emission rates from multiple sources using Bayesian probability theory. *Journal of Environmental Monitoring*, 12(3):622–634, 2010.

[92] Eric J Zhang, Chu C Teng, Theodore G van Kessel, Levente Klein, Ramachandran Muralidhar, Gerard Wysocki, and William MJ Green. Field deployment of a portable optical spectrometer for methane fugitive emissions monitoring on oil and gas well pads. *Sensors*, 19(12):2707, 2019.

[93] Xiaochi Zhou, Seungju Yoon, Steve Mara, Matthias Falk, Toshihiro Kuwayama, Travis Tran, Lucy Cheadle, Jim Nyarady, Bart Croes, Elizabeth Scheehle, et al. Mobile sampling of methane emissions from natural gas well pads in California. *Atmospheric Environment*, 244:117930, 2021.